Special Feature: Metallic Materials

Research Report

High Strength Fe-Ni-Co-Ti Alloy

Shigeru Kuramoto, Tadahiko Furuta, Naoyuki Nagasako and Zenji Horita

Report received on Jul. 3, 2012

ABSTRACT It is well known that the ideal strength of crystalline metallic materials is far beyond their actual strength, which can be explained by well-established dislocation theory. The theory describes that they deform with the aid of crystal defects called dislocations before the applied stress increases up to the stress level which can cause ideal shear. As a result, actual deformation strength of ordinary metals and alloys is generally decreased to 1/30-1/20 of their ideal tensile strength. We recently have shown that an ultrahigh strength Fe-Ni-Co-Ti alloy with enhanced ductility, whose strength is approaching ideal strength and being twice as much as the upper limit of conventional alloys, can be realized by introducing the paradox concept of lattice softening. Designing atomic arrangement with specific electronic structure creates the lattice softening, and a nanograined structure is then produced by subsequent processing with severe plastic deformation (SPD). We also have investigated microstructural evolution during SPD process by electron backscatter diffraction analysis using the Fe-Ni-Co-Ti alloy. In this article, our recent researches on the high strength Fe-Ni-Co-Ti alloy are summarized with a focus on our alloy design approach to control the atomic bonding of the metallic crystalline materials.

KEYWORDS Iron Based Alloy, Ultrahigh Strength, Ductility, Elastic Softening, Grain Refinement

1. Introduction

It is well known that the ideal strength of crystalline metallic materials is far beyond their actual strength, which can be explained by well-established dislocation theory.[1-3] The theory describes that they deform with the aid of crystal defects called dislocations before the applied stress increases up to the stress level which can cause ideal shear. As a result, actual deformation strength of ordinary metals and alloys is generally decreased to 1/30-1/20 of their ideal tensile strength. Macroscopic engineering strength of materials is often represented by elastic modulus and fracture strength. The modulus is the stress required to move atoms apart from their equivalent positions in the range that enables returning to the original positions upon unloading. The fracture strength is the stress required to completely separate the atoms from the nearest neighbor atoms. Both of them are determined by bonding strength of atoms in the material; the material with stronger atomic bonding generally shows higher elastic modulus and fracture strength.

We recently have shown that an ultrahigh strength Fe-Ni-Co-Ti alloy with enhanced ductility, whose strength is approaching ideal strength and being twice as much as the upper limit of conventional alloys, can be realized by introducing the paradox concept of lattice softening.[4] Designing atomic arrangement with specific electronic structure creates the lattice softening, and a nanograined structure is then produced by subsequent processing with severe plastic deformation (SPD). We also have investigated microstructural evolution during SPD process by electron backscatter diffraction (EBSD) analysis using the Fe-Ni-Co-Ti alloy.[5] In this article, our recent researches on the high strength Fe-Ni-Co-Ti alloy are summarized with a focus on our alloy design approach to control the atomic bonding of the metallic crystalline materials.

2. Experimental Procedure

An Fe-18.1%Ni-34.9%Co-9.3%Ti (in mass %) alloy was melted using high purity raw metals and cast in an iron mold under argon atmosphere. The ingot was hot-forged at 1,423 K into a round bar with 15 mm

diameter. The bar was then solution treated at 1,373 K for 86.4 ks in an argon atmosphere, and quenched in water. Disc specimens of 10 mm diameter and 0.8 mm height, h, for high-pressure torsion (HPT),[6,7] known as a typical SPD process, were prepared from the solution-treated bar. A disc specimen was placed between upper and lower anvils and torsion-strained by rotating the lower anvil at a rotation speed of 1 rpm under a compression stress of 6 GPa, for a selected number of turns, N, equal to 0.5, 1, 5, and 10 at room temperature. Here, the equivalent strain, ε, was calculated using the following relation:

$$\varepsilon = 2\pi Nr/h3^{1/2}, \quad \cdots\cdots\cdots\cdots\cdots\cdots (1)$$

where r is the distance from the disc center.[8] Mechanical properties were evaluated by hardness measurement and tensile test. Microstructural characterization was conducted using transmission electron microscopy (TEM), scanning electron microscopy (SEM), x-ray diffraction (XRD) and EBSD. The areas for EBSD analysis were selected from the regions of 0.4 mm height on the radial cross-sectional plane after N = 0.5 and 1. Experimental details are found elsewhere.[4,5]

3. Results and Discussion

3. 1 Mechanical Properties

Figure 1 shows changes in hardness with distance from the disc center. The hardness of the solution-treated specimen is 3.5 GPa and this is indicated by the horizontal dotted line. The hardness in the specimen after N = 1 gradually increases with distance from the disc center and appears to saturate at 3.5 mm to a hardness of 6-7 GPa. For the specimen of N = 5, tendency of hardness distribution is similar to the specimen of N = 1, but the distance for the saturation becomes shorter and the hardness level for the saturation increases to about 8 GPa. The hardness after N = 10 remains approximately constant from the center to the edge of the disc. The hardness values in Fig. 1 are re-plotted as a function of equivalent strain in **Fig. 2**, where the phases analyzed by XRD are also indicated. The solution-treated specimen consists of a γ phase with face-centered cubic (fcc) crystal structure. It is clear that the hardness increases up to 7 GPa in the early stage of straining (ε = 20-30) with the transformation from γ to α phase with body-centered cubic (bcc) crystal structure, and subsequently reaches a steady state where the hardness remains almost unchanged in the α phase with further straining.

Figure 3(a) shows the relation between ultimate tensile strength (*UTS*) and Young's modulus (E) of the specimens after N = 10 (ε = 113). The figure also plots for an ultrahigh strength titanium base alloy, called Gum Metal.[8] As shown in Fig. 3(a), the values for the conventional high strength alloys are on the line of UTS/E = 0.011, which shows the upper limit of the strength of the conventional crystalline alloys. The upper limit is considerably lower than ideal tensile strength, UTS/E = 0.05[9] which we use here as a rough

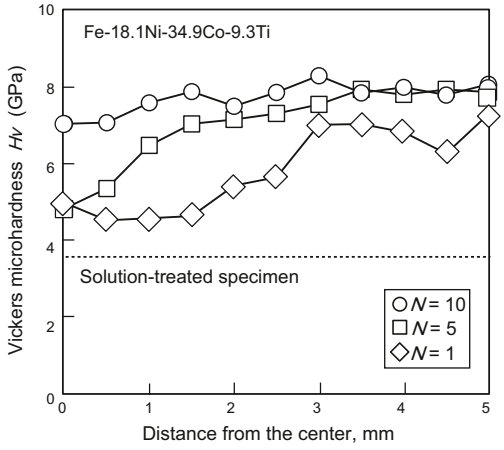

Fig. 1 Radial distributions of Vickers microhardness in the SPDed Fe-Ni-Co-Ti discs produced by HPT at rotation speed of 1 rpm for N turns at room temperature.

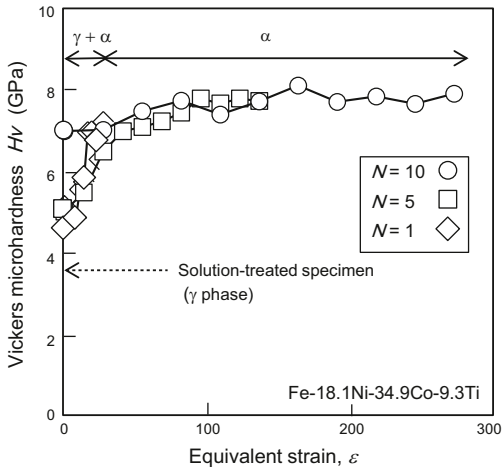

Fig. 2 Vickers microhardness as function of equivalent strain after HPT along with observed phases by XRD.

estimation for simplicity. The lower *UTS*/*E* value of the alloys, only 22% of the ideal one, can be explained by the dislocation theory.[1-3] It is noted that the present iron base alloy and Gum Metal have ultrahigh strength which is about twice as much as the conventional alloy, exhibiting 36% of the ideal strength.

There is a similarity in their crystal stability between these two alloys. It has been reported that the strengthening mechanism in Gum Metal[10-18] is different from the conventional crystalline alloys in which dislocation mechanism governs the whole mechanical behavior. In order to obtain high strength iron base alloy similar to Gum Metal, we determined the chemical composition of the present iron base alloy to realize a crystal stability similar to the one in Gum Metal.[19] Figure 3(b) shows schematically the relation between the lattice softening and the crystal stability. For the case of Gum Metal, phase 1 and 2 are hexagonal close-packed structure and bcc structure, respectively, and C'_{min} is 12.5-13.5 GPa at critical valence electron number, V_c, of 4.24.[17] The phase stability in the present iron alloy lies at the boundary where phase 1 and phase 2 are fcc structure and bcc structure, respectively. The Fe-Ni binary system has similar lattice softening in which C'_{min} is 21.5 GPa at critical valence electron number, V_c, of 8.75.[20] It has also been reported that significant lattice softening occurs in an Fe-Ni-Co-Ti alloy with transformation temperature near ambient temperature.[21] We found that V_c in the Fe-Ni-Co-Ti system lies at 8.40 where C'_{min} is attained, and determined the chemical composition to meet this criterion.

Figure 4(a) shows the initial part of stress-strain relationship during tensile loading in the specimen after $N = 10$; it also includes one in Gum Metal. The elastic deformability of the iron alloy is as much as 1.8%, which is similar to that in Gum Metal,[8] and considerably higher than conventional metallic alloys with less than 0.5%. This specimen started to deform plastically after the elastic limit and the applied stress increased up to maximum of 2,733 MPa and then decreased to fracture at 2,160 MPa with a total elongation to fracture of 9.4%, which is considered to be sufficient ductility for ordinary industrial products. Figure 4(b) shows the fracture surface after tensile separation, which is characterized by very fine and uniform distribution of microdimples. The microdimples confirm that this specimen failed after substantial amount of local plastic deformation accompanied by ductile process of microvoid evolution and coalescence. Figure 4(c) presents the relationship between *UTS*/*E* and elongation for high strength iron base alloys including lab-based special alloys [22,23] and thin steel wires.[24,25] This figure also contains the plots for iron base metallic glasses [26] and SPD-processed (SPDed) pure metals with fine grain structures.[27,28] The precipitation hardened Fe-Mo base laboratory alloys have the highest strength among the bulk iron base alloys ever reported,[22,23] and they have very high value of *UTS*/*E* but with poor ductility. Iron

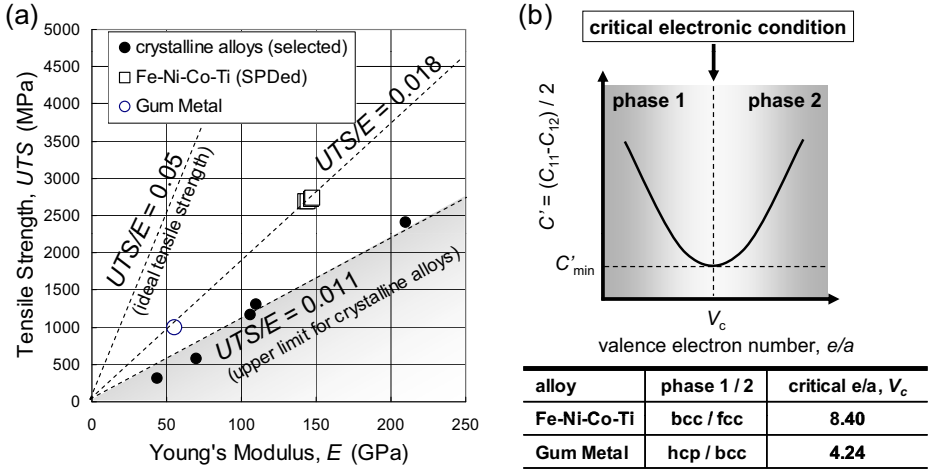

alloy	phase 1 / 2	critical e/a, V_c
Fe-Ni-Co-Ti	bcc / fcc	8.40
Gum Metal	hcp / bcc	4.24

Fig. 3 (a) Plots of the ultimate tensile strength (UTS) vs. Young's modulus (E) for the SPDed Fe-Ni-Co-Ti alloy after 10 turns of HPT, an ultrahigh-strength titanium alloy called Gum Metal, and other selected high-strength crystalline metallic alloys. (b) Schematic representation of lattice softening at the limit of phase stability, in which we referred to the data of elastic constants for Fe-Ni binary alloys.

base metallic glasses have similar properties to the Fe-Mo alloys, however they are very brittle like other glasses. Some of the cold drawn thin wires[24,25] have the better combination of strength and ductility than the Fe-Mo alloys but their ductility is limited to no more than 3% of elongation. The dashed line in Fig. 4(c) indicates the maximum strength which can be achieved in conventional high strength iron base alloys. We can confirm that the present iron base alloy has definitely higher level for both strength and ductility beyond the properties of the conventional alloys.

3. 2 Microstructure Evolution during HPT Straining

Since the hardness increases in the early stage of HPT processing (ε = 20-30), it is important to study the changes in microstructure with equivalent strain ranging from ε = 0 to 30 to understand the strengthening behavior of the present iron base alloy. **Figure 5** shows SEM images along with inverse pole figure (IPF) maps for both γ and α phases obtained from the EBSD analysis. In Figs. 5(a)-(c) at ε = 0.45, the microstructure consists of slightly elongated γ grains with the average grain size of 100-200 μm, being not much different in grain size from the initial state of the solution-treated specimen. In Figs. 5(d)-(f) at ε = 3.4, a lamellar microstructure appears by further HPT straining. It is clear from the results of crystal orientation analysis by EBSD in Figs. 5(e), (f) that the lamellar-shaped α phase was generated in the γ grains by stress-induced martensitic transformation during HPT. **Figure 6** shows the results of detailed analysis on orientation relationship between the initial γ and the induced α. It is apparent from the pole figures that ND of the induced α phase is almost aligned to (110). Although there is some amount of misorientation, the orientation relationship between the γ and α phases is almost (111)γ // (110)α. Further orientation analysis from several observed areas exhibited that the habit plane of the transformation is close to (111)γ, and that the orientation between the γ and the α is Kurdjumov-Sachs (K-S) relationship, (111)γ // (011)α, <0-11>γ // <1-11>α. As indicated in Figs. 5 and 6, the lamellar-shaped α phase extends through the whole γ grain with the sizes of 100-200 μm, and the crystal orientation in the induced α phase appears to be aligned in the specific direction as seen in IPF map (Fig. 5(f)).

The pole figure (Fig. 6(d)) shows that there is some amount of misorientation in the α phase, and variants of α phase from two different habit planes appear in the IPF map (Fig. 5(f)). Hence, further analysis was made on the induced α phase to determine the detailed

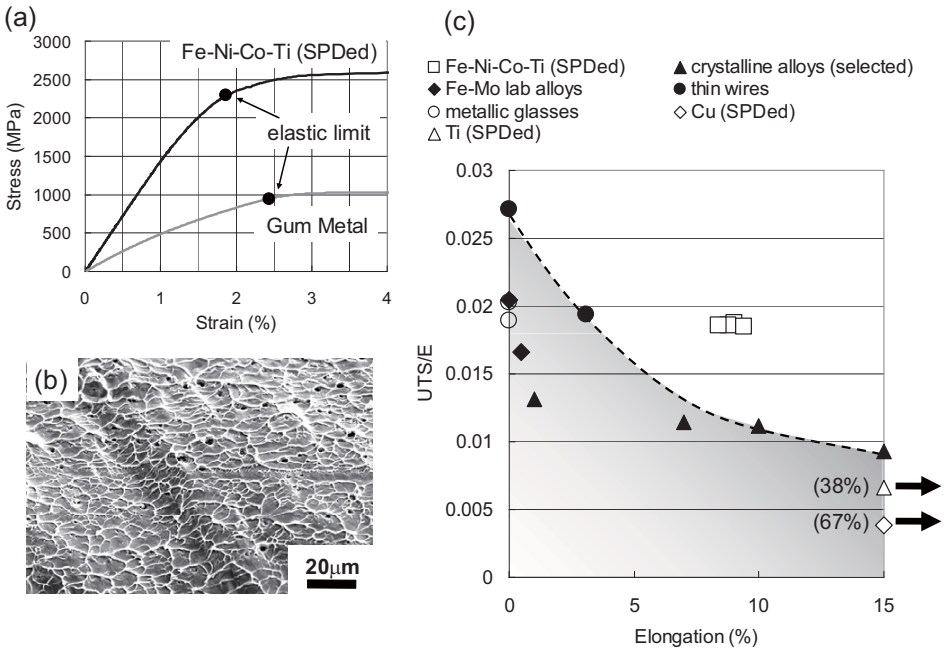

Fig. 4 (a) Stress-strain curves for the SPDed Fe-Ni-Co-Ti alloy and Gum Metal. (b) Scanning electron micrograph of the fractured surface of the SPDed Fe-Ni-Co-Ti alloy. (c) Plots of the UTS/E vs. elongation for the Fe-Ni-Co-Ti alloy and the other high strength iron base alloys.

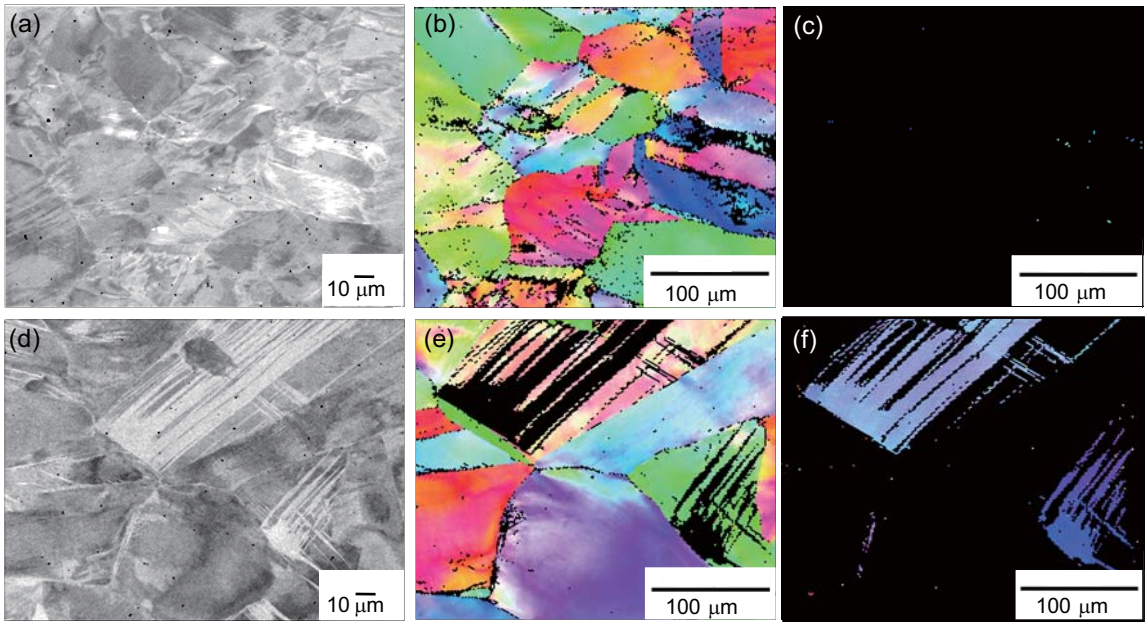

Fig. 5 Microstructure after HPT for $N = 0.5$. (a, d) SEM images, (b, e) IPF maps for γ phase, and (c, d) IPF maps for α phase. (a, b, c) at region of 0.2 mm and (d, e, f) of 1.5 mm from center.

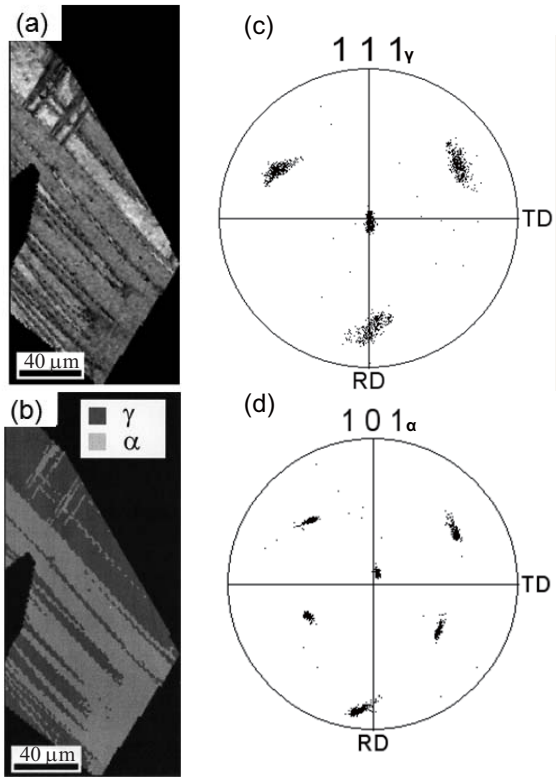

Fig. 6 Orientation analysis on relationship between initial γ and stress-induced α in region 0.2 mm from center after HPT for $N = 0.5$. (a) Image quality map, (b) γ and α phase map, and pole figures (c) for (111)γ and (d) for (110)α.

orientation distribution after the phase transformation, as shown in **Fig. 7**. Here, the orientation variation, by about 10 degrees, is indicated by color gradation. The orientation in the α phase in Fig. 7(a) changes gradually from the lower right to the upper left direction. Figure 7(c) shows misorientation profiles along the arrow shown in Fig. 7(a). The misorientation profiles indicate that the misorientation angle between the lower right region and the upper left is about 10 degrees, and the orientation gradually changes between the two regions. This misorientation can be seen on the pole figure in Fig. 7(b), and is understood by considering two different habit planes for the transformation. In cubic crystals, the angle of neighboring {111} is 70.5 degrees and that of neighboring {110} is 60 degrees. So, if two different variants are transformed from the same initial γ grain, the resultant misorientation between the two variants in the α phase would be 10.5 degrees since the γ phase and the transformed α phase have the K-S relationship (Fig. 7(d)). This misorientation of 10 degrees well coincides with the misorientation observed from EBSD analysis (Fig. 7(c)) and it can be concluded that stress-induced phase transformation from the γ to the α generates a specific amount of crystal rotation inside the grain due to transformation from different habit planes. It has been reported that there are 24 variants in the K-S relationship, and six variants are expected

to be generated from one parent γ grain.[29] The misorientation angles between the six variants are 10.5, 49.5, or 60 degrees. Only the variants having the misorientation of 10.5 degrees were observed in this study, however, there possibly exist the variants with the other misorientation angles. Meanwhile, similar crystal rotation was also found in the γ phases (shown by an arrow in Fig. 5(e)), which have not transformed yet.

Figure 8 shows crystal structure and microstructures after $N = 10$ ($\varepsilon = 113$). Initial crystal structure of the alloy before HPT is γ phase with fcc structure, which totally transforms into α phase with bcc structure during the HPT process (Fig. 8(a)). The HPT process also changes the grain structure of the alloy; initial grain size of the alloy was about 200 μm, but the HPT process causes significant grain refinement, resulting in a very fine grain structure, as shown in Figs. 8(b)-(d). The average grain size appears to be 20-50 nm, and there seems to be high density of crystal defects inside the grains. Such significant structural refinement was observed throughout the specimen, which has never been reported before in bulk iron base alloys. This significant grain refinement along with high density of defects should be responsible for suppression of the dislocation motion up to ultrahigh stress level. There have been a number of reports on microstructural refinement by SPD process, where an enormous amount of dislocations introduced during SPD process are believed to contribute to the formation of high density of grain boundaries. However, the reported grain sizes are of one order of magnitude larger than the one in the present study.[30,31] **Figure 9** summarizes the grain size in the γ and α phase as a function of the equivalent strain. The initial grain size of the γ phase, 200-300 μm, decreases with increasing equivalent strain, and it reaches the size of 500 nm at $\varepsilon = 3.4$. The initial γ phase completely transformed to the α phase up to $\varepsilon = 15.4$ and it was not observed for further straining. The α phase was found at $\varepsilon = 3.4$ and increases the fraction with increasing equivalent strain until it reaches the size of 20-50 nm at $\varepsilon = 113$.

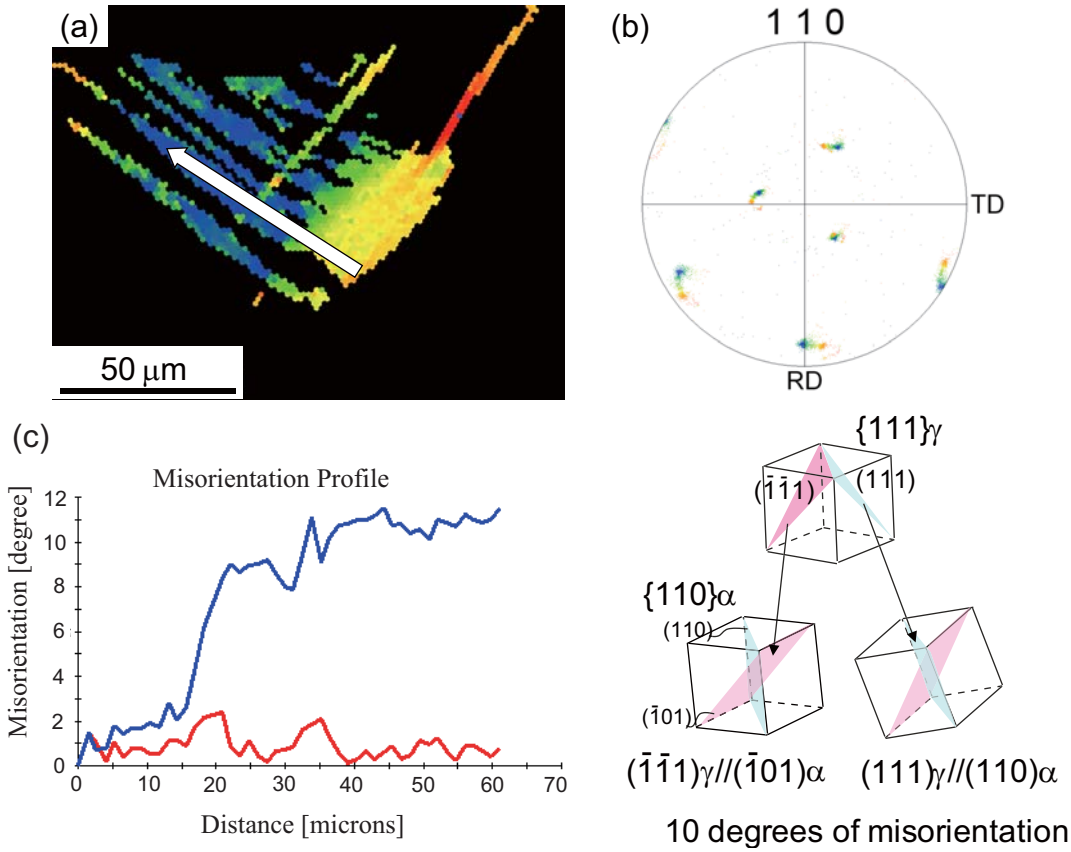

Fig. 7 Detailed orientation map and corresponding pole figure of stress-induced α phase in region 0.2 mm from center after HPT for $N = 0.5$. (a) Orientation map for a phase and (b) pole figure for {110}α, (c) misorientation along arrow in (a), and (d) schematic of orientation relationships between {111}γ and {110}α.

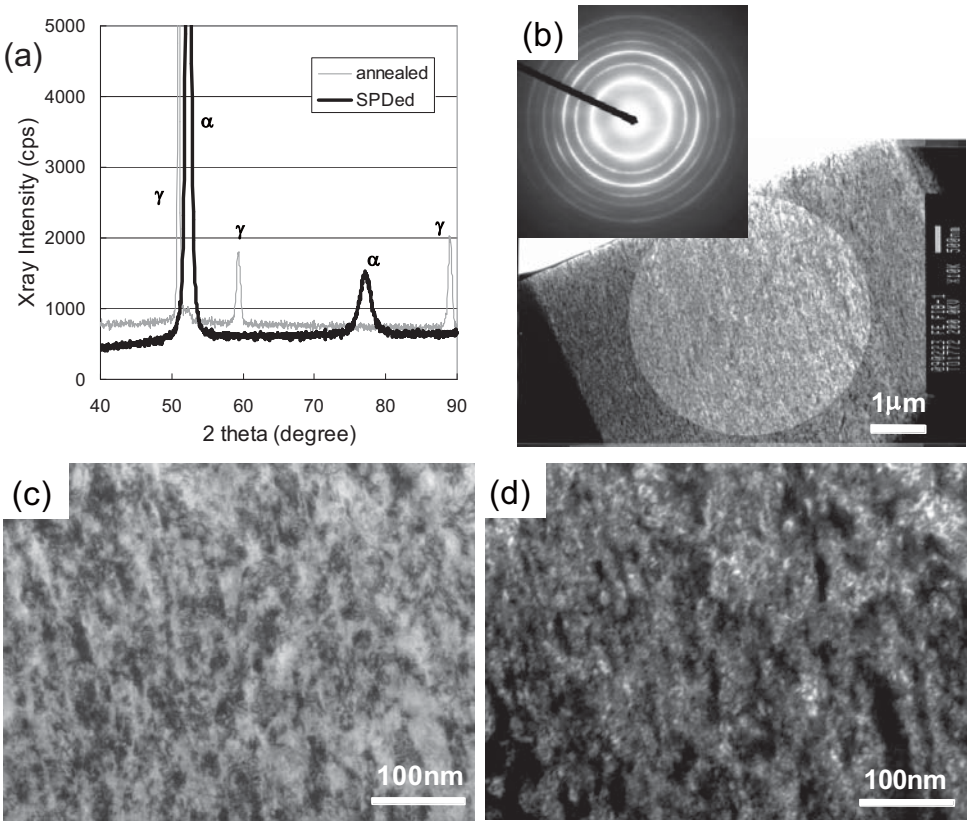

Fig. 8 (a) X-ray profiles of the Fe-Ni-Co-Ti alloy before and after SPD. (b) Transmission electron micrograph and selected area diffraction pattern of the Fe-Ni-Co-Ti alloy after SPD. (c) Bright-field image enlarged from Fig. 8(b). (d) Dark-field image enlarged from Fig. 8(b).

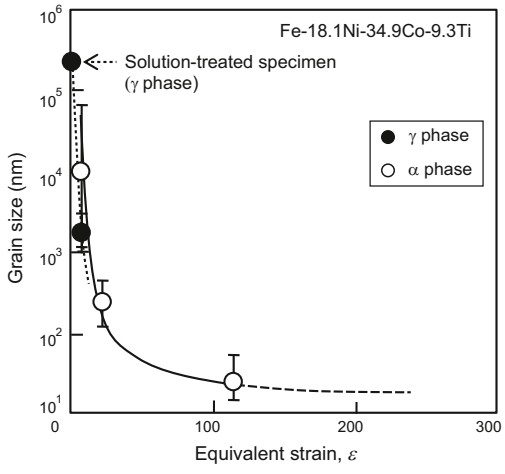

Fig. 9 Grain size in γ and α phase as function of equivalent strain after HPT.

3. 3 Deformation Mechanism and Grain Refinement Behavior

From the dislocation theory, the strength of an alloy can be increased if dislocation motion is suppressed by fine second phase particles generated by precipitation heat treatment or high density of dislocations accumulated during heavy cold working. At the same time, dislocations are media of plastic flow in metallic crystalline alloys, so that high strength alloys always tend to have low ductility, because dislocations are suppressed to move to relax the accumulated strain by loading. Figure 4(c) shows that the *UTS*/*E* ratio and elongation of Gum Metal are 0.018 and 10%, respectively, and this balance of mechanical strength and ductility is almost identical to that of the iron base alloy. Hence, we consider that the deformation mechanism in the present iron base alloy is similar to that in Gum Metal,[8,10-18] in which ideal shear deformation appears to govern local plastic deformation process instead of conventional dislocation mediated plasticity. Such dislocation free deformation mechanism could account for the unusual

mechanical behavior of the present iron alloy.

Let us consider the ideal shear strength, τ_{Ideal}, which is the theoretical shear strength for perfect bcc crystals [32] in order to discuss the possible deformation mechanism of the present iron-based alloy. Here, τ_{Ideal} can be roughly estimated to be 3.2 GPa by using elastic constants of an Fe-36.5 at.%Ni binary alloy [20] with similar lattice softening to the present iron-based alloy. The actual shear stress, τ_{Actual}, in the present iron-based alloy can be estimated as 1.37 GPa,[33] and the ratio of the τ_{Actual} to τ_{Ideal} is 38%. The ratio for Gum Metal is 36% and this is almost the same as that of the present iron-based alloy. In the case of ordinary metals and alloys, the τ_{Actual} is generally decreased to 1/30-1/20 of the τ_{Ideal} but the ratio of τ_{Actual} / τ_{Ideal} for the present iron-based alloy and Gum Metal is much higher than the ordinary metals. Although the macroscopic stress applied during plastic deformation is lower than the ideal strength in Gum Metal, it is considered that the significant stress concentrations increase local applied stress and enables the deformation near ideal strength.[34] In the case of Gum Metal, very strong pinning of dislocation operates up to the ideal shear strength by fine obstacles.[12,15,16,18] On the other hand, it has been reported that grain refinement is very effective to suppress the dislocation motion, and the bcc iron with grain sizes of 20-50 nm is estimated to have deformation stress of 2.3-3 GPa.[35] Therefore we consider that dislocation motion is suppressed up to ideal strength level by dense distribution of grain boundaries and other crystal defects in the interior of the grains in the present iron base alloy (Figs. 8(c) and (d)). Hence, the rough estimation here implies that the strength of the present iron-based alloy produced by HPT is approaching ideal shear strength. Such a mechanism free from dislocation activity at ideal strength may be related to the improved ductility of the present iron-based alloy, and would also explain the mechanism for the significant grain refinement.

The grain refinement process can be divided, from Figs. 2 and 9, into two steps: the first one for the early stage with significant hardening from $\varepsilon = 0$ to $\varepsilon = 20$ and the second one for the later stage with moderate hardening from $\varepsilon = 20$ to $\varepsilon = 100$. The initial hardness and the final saturated hardness value are 3.5 and 8 GPa, respectively. The results shown in Figs. 5, 6, and 7 indicate that the changes in microstructure occur in the very early stage of hardening. In the very early deformation stage until $\varepsilon = 5$, there are two kinds of grain refinement processes from initial γ grain with the sizes of 200-300 μm. One case of the grain refinement is based on the crystal lattice rotation generated by the deformation-induced martensitic transformation from γ to α. Although the rotation angle of about 10 degrees is not enough to make high angle grain boundaries, such low angle orientation gaps would evolve into grain boundaries with higher misorientation angles through subsequent HPT straining. In addition, rearrangements of the variants in the α phase also possibly make new boundaries with 49.5 or 60 degrees [29] during the subsequent HPT straining. The other case is the grain refinement caused by lattice rotation in the initial γ phase shown in Fig. 5(e). This observation suggests that the α phase is refined after stress-induced transformation, since several number of α variants would be generated upon the transformation from the γ phase with such orientation variation.

The mechanism of grain refinement in the later stage of HPT straining is considered to be different from ones described above. Generally, structural transformation [36] or deformation twinning [37] during SPD process has an effect on significant grain refinement; these types of grain refinement are accompanied by cooperative movement of a group of atoms, which is different from gradual structural changes in local area by dislocation motion.[36] In the lattice softened alloys like Gum Metal and the present iron-based alloy, localized elastic softening occurs along <111> direction, which is the easy glide direction in bcc crystals. When the local stress is increased nearly equal to the ideal shear strength with the aid of some stress concentrations, a transgranular shear could proceed spontaneously across the maximum shear stress plane. Such transgranular shear can contribute to the grain division in α grains in the present case. The hardness of the specimen at equivalent strain of 15.4 was 7 GPa (Fig. 2), which is 88% of the saturated hardness value of 8 GPa. Thus, the applied stress is considered to be high enough to exert the deformation mechanism without dislocation activity in the later stage of HPT straining. The deformation mechanism of the present iron-based alloy along with the grain refinement mechanism will have to be investigated further by critical characterization of microstructure during HPT process.

4. Conclusions

Mechanical properties and microstructure of an Fe-Ni-Co-Ti based crystalline alloy were summarized

and deformation mechanism and grain refinement behavior were discussed. The alloy exhibits twice the upper limit strength as an equivalent conventionally processed alloy. It also exhibited substantial ductility of 8-10% of tensile elongation. The initial microstructure of the alloy consisted of coarse γ grains, in which lamellar-shaped α phase was induced by martensitic transformation in the early stage of HPT straining. Subsequent straining in the later stage of HPT generated very fine α grains with the size of 20 to 50 nm. The mechanism of this significant grain refinement throughout the specimen was discussed in relation to martensitic transformation and transgranular shear near ideal strength. The unusual mechanical strength was achieved by careful selection and control of atomic arrangement and nanostructure in the alloy. The deformation mechanism of the alloy cannot be understood by the conventional theory for crystal deformation, and it seems to deform at the strength level near ideal strength. Such a deformation mechanism can explain the ultrahigh strength along with good ductility as well as the significant grain refinement in the present iron-based alloy. We think that the present result leads to an important technology for developing ultrahigh strength alloys, which can change the concept of production process of metallic materials.

This study was performed in cooperation with T. Ohsuna, K. Horibuchi, N. Suzuki, A. Yamada and M. Sawamura in Toyota Central R&D Labs., Inc. for characterization of microstructure, evaluation of mechanical properties and technical assistance on HPT processing.

References

(1) Taylor, G. I., *Proc. Roy. Soc. A*, Vol.145 (1934), p.362.
(2) Orowan, E., *Zeit. Phys.*, Vol.89 (1934), p.605.
(3) Polanyi, M., *Zeit. Phys.*, Vol.89 (1934), p.660.
(4) Kuramoto, S., et al., *Appl. Phys. Lett.*, Vol.95 (2009), 211901.
(5) Furuta, T., et al., *J. Mater. Sci.*, Vol.45 (2010), p.4745.
(6) Valiev, R. Z., et al., *JOM,* Vol.58 (2006), p.33.
(7) Bridgman, P. W., *Studies in Large Plastic Flow and Fracture* (1952), McGraw-Hill.
(8) Saito, T., et al., *Science*, Vol.300 (2003), p.464.
(9) Ashby, M. F. and Greer, A. L., *Scr. Mater.,* Vol.54 (2006), p.321.
(10) Kuramoto, S., et al., *Metall. Mater. Trans. A,* Vol.37A (2006), p.657.
(11) Gutkin, M. Y., et al., *Acta Mater.,* Vol.54 (2006), p.2489.
(12) Li, T., et al., *Phys. Rev. Lett.*, Vol.98 (2007), 105503.
(13) Bobylev, S. V., et al., *Phys. Rev. B*, Vol.77 (2008), 094115.
(14) Gutkin, M. Y., et al., *Int. J. Plasticity*, Vol.24 (2008), p.1333.
(15) Withey, E., et al., *Mater. Sci. Eng. A*, Vol.493 (2008), p.26.
(16) Withey E. A., et al., *Experimental Mechanics*, Vol.50 (2010), p.37.
(17) Hara, M., et al., *Int. J. Mater. Res.*, Vol.100 (2009), p.345.
(18) Yano, T., et al., *Acta Mater.*, Vol.57 (2009), p.628.
(19) Ikehata, H., et al., *Phys. Rev. B*, Vol.70 (2004), 174113.
(20) Every, G. and McCurdy, A. K., *Landolt-Börnstein*, Vol.29 (1992), p.29, Springer-Verlag.
(21) Cesari, E., et al., *Scr. Mater.*, Vol.40 (1999), p.341.
(22) Muneki, S., et al., *Testu-to-Hagane* (in Japanese), Vol.69 (1983), p.2030.
(23) Mihalisin, J. R. and Bieber, C. G., *J. Metals*, Vol.18 (1966), p.1033.
(24) Ochiai, I., et al., *Testu-to-Hagane* (in Japanese) Vol.79 (1993), p.1101.
(25) Oki, Y., et al., *Kobe Steel Engineering Report*, Vol.50 (2000), p.37.
(26) Inoue, A., et al., *Acta Mater.*, Vol.52 (2004), p.4093.
(27) Valiev, R., *Nature Mater.*, Vol.3 (2004), p.511.
(28) Whang, Y., et al., *Nature*, Vol.419 (2002), p.912.
(29) Morito, S., et al., *Acta Mater.*, Vol.51 (2003), p.1789.
(30) Wetscher, F., et al., *Mater. Sci. Eng. A*, Vols.387-389 (2004), p.809.
(31) Edalati, K., et al., *Mater. Trans.*, Vol.50 (2009), p.44.
(32) Krenn, C., et al., *Mater. Sci. Eng. A*, Vols.319-321 (2001), p.111.
(33) Furuta, T., et al., *Proc. of the 2nd Int. Symp. Steel Science* (*ISSS 2009*), (2010), The Iron and Steel Institute of Japan.
(34) Kuramoto, S., et al., *Mater. Sci. Forum*, Vols.638-642 (2010), p.3858.
(35) Takaki, S., et al., *J. Mater. Proc. Technol.*, Vol.117 (2001), p.359.
(36) Tsuji, N. and Maki, T., *Scr. Mater.*, Vol.60 (2009), p.1044.
(37) Zhao, Y. H., et al., *Mater. Sci. Eng. A*, Vol.493 (2008), p.123.

Shigeru Kuramoto

Research Field:
- Deformation and Fracture in Metallic Materials

Academic Degree: Dr.Eng.

Academic Societies:
- The Japan Institute of Metals
- The Iron and Steel Institute of Japan
- The Japan Institute of Light Metals
- The Minerals, Metals & Materials Society

Awards:
- Light Metal Paper Prize, The Japan Institute of Light Metals, 2002
- The Japan Institute of Metals Technical Development Award, 2004

Tadahiko Furuta

Research Field:
- Mechanical Evaluation and Process Development of Metallic Materials

Academic Degree: Dr.Eng.

Academic Societies:
- The Japan Institute of Metals
- The Iron and steel Institute of Japan
- The Minerals, Metals & Materials Society

Awards:
- The Japan Institute of Metals Technical Development Award, 1995
- R&D 100 Award, 1996
- JSMS Award for Technical Developments, The Society of Materials Science, Japan, 1999
- Japan Powder Metallurgy Association New Products Award, 2001
- The Japan Institute of Metals Technical Development Award, 2004

Naoyuki Nagasako

Research Field:
- Computational Physics and Its Application to Materials Design

Academic Degree: Dr.Sci.

Academic Societies:
- The Physical Society of Japan
- American Physical Society
- The Japan Institute of Metals

Zenji Horita*

Research Field:
- Nanostructural Refinement for Advanced Materials Using Giant Straining Process

Academic Degrees:
- Ph.D.
- Dr.Eng.

Academic Societies:
- The Japan Institute of Metals
- The Iron and Steel Institute of Japan
- The Japan Institute of Light Metals
- The Japanese Society for Heat Treatment
- The Japanese Society of Microscopy
- American Institute of Mining, Metallurgical and Petroleum Engineers

Awards:
- Light Metal Encouragement Prize, The Japan Institute of Light Metals, 1984
- The Japan Institute of Metals Meritorious Award, 1999
- Seto Award, The Japanese Society of Microscopy, 1999
- Sōmiya Award, The International Union of Materials Research Societies (IUMRS), 2005
- Light Metal R&D Furtherance Medal, The Japan Institute of Light Metals, 2011

*Kyushu University

